

submitted to *Geophys. J. Int.*

# **Magnetic radial inversion for 3-D source geometry estimation**

L.B. Vital<sup>1\*</sup>, V.C. Oliveira Jr.<sup>1</sup> and V.C.F. Barbosa<sup>1</sup>

<sup>1</sup> *Observatório Nacional, Gal. José Cristino, 77, São Cristóvão, Rio de Janeiro, 20921-400, Brazil*

**SUMMARY**

We present a method for inverting total-field anomaly data to estimate the geometry of a uniformly magnetized 3-D geological source in subsurface. The method assumes the total-magnetization direction is known. We approximate the source by an ensemble of vertically juxtaposed right prisms, all of them with the same total-magnetization vector and depth extent. The horizontal cross-section of each prism is defined by a polygon having the same number of vertices equally spaced from  $0^\circ$  to  $360^\circ$ . The position of these vertices, the horizontal location of each prism and the depth extent of all prisms are the parameters to be estimated by solving a constrained nonlinear inverse problem for minimizing a goal function. We run successive inversions for a range of tentative total-magnetization intensities and depths to the top of the shallowest prism. The estimated models producing the lowest values of the goal function form the set of candidate solutions. To obtain stable solutions, we impose the zeroth- and first-order Tikhonov regularizations on the shape of the prisms. The method allows estimating the geometry of both vertical and inclined sources by the suitable use of first-order Tikhonov regularization. Tests with synthetic data produced by simple and complex simulated bodies show the efficiency of our method in retrieving the shape of the magnetic source. Results obtained by inverting airborne total-field anomaly data over the Anitápolis alkaline-carbonatic complex, in the Santa Catarina state, Brazil, suggest that the emplacement of the magnetic sources was controlled by NW-SE-trending faults at depth, in accordance with known structural features at the study area.

**Key words:** Magnetic anomalies: modelling and interpretation; Inverse theory; Numerical solutions.

## 1 INTRODUCTION

The interpretation of total-field anomalies on the surface of the Earth is an important challenge in exploration geophysics due to the nonuniqueness of 3-D magnetic inversion. It is well-known that several magnetization distribution in subsurface can reproduce the same magnetic data with the same accuracy. To overcome this inherent ambiguity, a priori information need to be introduced for reducing the number of possible possible solutions that are coherent with the local geology. There are basically three groups of 3-D magnetic inversion methods. The available a priori information determines the suitable approach for each case.

The first group of methods approximates the source by a geometrically simple causative body having its geometry defined by a small number of parameters (e.g., Ballantyne 1980; Bhattacharyya 1980; Silva & Hohmann 1983). These methods estimate both the geometry and the physical property of the source by solving a nonlinear inverse problem. Due to the very restrictive parametrization, such methods usually do not have severe problems with ambiguity.

The second group is formed by the vast majority of methods. They approximate the subsurface by a grid of juxtaposed rectangular prisms having a constant total-magnetization direction. Some methods presume that a purely induced magnetization (e.g., Cribb 1976; Li & Oldenburg 1996; Pilkington 1997) and the isotropic magnetic susceptibility of the prisms is the quantity estimated by solving a linear inverse problem. Different approaches have improved this inversion method to obtain focused images of the subsurface. For example, Portniaguine & Zhdanov (1999) and Portniaguine & Zhdanov (2002) introduced the minimum gradient support to minimize the effect of strong variations and discontinuity on the parameters by inverting magnetic anomaly and any component of the total anomalous field. Barbosa & Silva (2006) presented a method for inverting interfering magnetic anomalies by combining features of the forward modeling (the interactivity) and traditional inversion (the automatic data fitting). Other studies introduced strategies to constraint the nonuniqueness and delineate the source (Caratori Tontini et al. 2006; Pilkington 2009; Shamsipour et al. 2011; Cella & Fedi 2012; Abedi et al. 2015). Exceptionally, some of these methods allowed different magnetization direction from the local main field one (e.g., Pignatelli et al. 2006). In this case, the parameters to be estimated are the total-magnetization intensities of the prisms. In all these methods, and thus, the geometries of the magnetic sources are indirectly retrieved by interpreting the estimated total-magnetization intensity distribution. Theoretically, these inversion methods are capable of recovering the geometry of complex sources. However, they require a plethora of a priori information to overcome their nonuniqueness and instability due to the large number of parameters to be estimated. Additionally, they are characterized by a high computational cost associated due to the solution of large linear systems.

The third group of 3-D magnetic inversion methods presume some knowledge about the phys-

ical property distribution and estimate the geometry of the sources. They are usually formulated as nonlinear inverse problems. Wang & Hansen (1990) approximate the source by a polyhedron and estimate the position of its vertices in the Fourier domain. Li et al. (2017) have developed a multiple level-set method to estimate geometry of a set of causative bodies with uniform magnetic susceptibility. Hidalgo-Gato & Barbosa (2019) inverted the total-field anomaly for estimating the geometry of a basement relief of a sedimentary basin with known magnetization intensity but unknown magnetization direction. This method has a small number of parameters to be estimated by inversion and much less ambiguity in comparison to the second group.

We present a magnetic inversion to estimate the geometry of an isolated and uniformly 3-D magnetic source having known total-magnetization direction. Our method is an extension for total-field anomaly data of those methods presented by Oliveira Jr. et al. (2011) and Oliveira Jr. & Barbosa (2013) for inverting gravity and gravity-gradient data, respectively. We approximate the source by an interpretation model formed by vertically juxtaposed right prisms having horizontal cross-sections defined by polygons, all of them with the same number of vertices. For convenience, all prisms have the same thickness and total-magnetization intensity. Differently from Oliveira Jr. et al. (2011) and Oliveira Jr. & Barbosa (2013), our method estimates not only the horizontal Cartesian coordinates of the origins and the radii of the vertices describing the horizontal cross-sections of all prisms, but also the thickness of all prisms forming the interpretation model. Additionally, we perform a numerical analysis to investigate the sensitivity of our method to the use of different values of total-magnetization intensities and depths to the top of the shallowest prism. Among the estimated models, those producing the lowest values of goal function form the set of candidate models. To obtain a stable solutions, we use the same set of regularizing functions proposed by Oliveira Jr. et al. (2011) and also propose a new one for constraining the thickness of the prisms.

A test with synthetic data produced by a simple symmetric model shows the performance of our method in an ideal case. We also applied our method to interpret the synthetic data produced by a complex sources having variable shape and dip along depth. The results show that our method can be a very useful tool for interpreting magnetic data in real situations. Based on these synthetic tests, we applied our method to interpret airborne data over the alkaline-carbonatitic complex of Anitápolis, in the Santa Catarina state, in southern Brazil. Our results bring some light on the debate about the structural control of the Anitápolis complex. Our results suggest that the complex is an intrusion source dipping to northwest and maximum bottom depth of about 4 km, in agreement with known geological structures not only located at, but also northward and southward the study area.

## 2 METHODOLOGY

### 2.1 Forward problem

Let  $\mathbf{d}^o$  be the observed data vector, whose  $i$ th element  $d_i^o$ ,  $i = 1, \dots, N$ , is the total-field anomaly produced by a 3-D source (Fig. 1a) at the point  $(x_i, y_i, z_i)$  of a Cartesian coordinate system with  $x$ ,  $y$  and  $z$  axes pointing to north, east and down, respectively. We assume that the direction of the total magnetization vector of the source is constant and known. We approximate the volume of the source by a set of  $L$  vertically juxtaposed 3-D prisms (Fig. 1b) by following the same approach of Oliveira Jr. et al. (2011) and Oliveira Jr. & Barbosa (2013). The depth to the top of the shallowest prism is defined by  $z_0$  and  $m_0$  is the constant total-magnetization intensity of all prisms. The horizontal cross-section of each prism (Fig. 2) is described by a polygon with a fixed number  $V$  of vertices equally spaced from  $0^\circ$  to  $360^\circ$ , which are described in polar coordinates referred to an internal origin  $O^k$ . The radii of the vertices ( $r_j^k$ ,  $j = 1, \dots, V$ ,  $k = 1, \dots, L$ ), the horizontal coordinates ( $x_0^k$  and  $y_0^k$ ,  $k = 1, \dots, L$ ) of the origins  $O^k$ ,  $k = 1, \dots, L$ , and the thickness  $dz$  of the  $L$  vertically stacked prisms (Fig. 1b) are arranged in a  $M \times 1$  parameter vector  $\mathbf{p}$ ,  $M = L(V + 2) + 1$ , given by

$$\mathbf{p} = \begin{bmatrix} \mathbf{r}^{1\top} & x_0^1 & y_0^1 & \dots & \mathbf{r}^{L\top} & x_0^L & y_0^L & dz \end{bmatrix}^\top, \quad (1)$$

where “ $\top$ ” denotes transposition and  $\mathbf{r}^k$  is a  $V \times 1$  vector containing the radii  $r_j^k$  of the  $k$ th prism. Let  $\mathbf{d}(\mathbf{p})$  be the predicted data vector, whose  $i$ th element

$$d_i(\mathbf{p}) \equiv \sum_{k=1}^L f_i^k(\mathbf{r}^k, x_0^k, y_0^k, dz, z_1^k, m_0), \quad i = 1, \dots, N, \quad (2)$$

is the total-field anomaly produced by the ensemble of  $L$  prisms at the  $i$ th observation point  $(x_i, y_i, z_i)$ . In eq. 2,  $f_i^k(\mathbf{r}^k, x_0^k, y_0^k, dz, z_1^k, m_0)$  is the total-field anomaly produced, at the observation point  $(x_i, y_i, z_i)$ , by the  $k$ th prism, with depth to the top  $z_1^k = z_0 + (k - 1)dz$ . We calculate  $d_i(\mathbf{p})$  (eq. 2) by using the Python package Fatiando a Terra (Uieda et al. 2013), which implements the formulas proposed by Plouff (1976).

### 2.2 Inverse problem formulation

The total-magnetization of the source  $m_0$  and depth to the top of the shallowest prism  $z_0$  are hyperparameters of the inversion, i. e., they are not estimated during the inversion, but their value influences the final solution. Given a set of tentative values for  $m_0$  and  $z_0$ , we solve a constrained non-linear problem to estimate the parameter vector  $\mathbf{p}$  (eq. 1) by minimizing the goal function

$$\Gamma(\mathbf{p}) = \phi(\mathbf{p}) + \sum_{\ell=1}^7 \alpha_\ell \varphi_\ell(\mathbf{p}), \quad (3)$$

subject to

$$p_l^{min} < p_l < p_l^{max}, \quad l = 1, \dots, M, \quad (4)$$

where  $\phi(\mathbf{p})$  is the data-misfit function given by

$$\phi(\mathbf{p}) = \frac{1}{N} \|\mathbf{d}^o - \mathbf{d}(\mathbf{p})\|_2^2, \quad (5)$$

which represents the normalized squared Euclidean norm of the difference between the observed data vector  $\mathbf{d}^o$  and the predicted data vector  $\mathbf{d}(\mathbf{p})$ ,  $\alpha_\ell$  is a positive number representing the weight of the  $\ell$ th constraint function  $\varphi_\ell(\mathbf{p})$  and  $p_l^{min}$  and  $p_l^{max}$  are, respectively, the lower and upper limits for the  $l$ th element  $p_l$  of the parameter vector  $\mathbf{p}$  (eq. 1). These limits are defined by the interpreter based on both the horizontal extent of the magnetic anomaly and the knowledge about the source.

To solve our nonlinear inverse problem, we use a gradient-based method and, consequently, we need to define the gradient vector  $\nabla\Gamma(\mathbf{p})$  and Hessian matrix  $\mathbf{H}(\mathbf{p})$  of the goal function  $\Gamma(\mathbf{p})$  (eq. 3):

$$\nabla\Gamma(\mathbf{p}) = \nabla\phi(\mathbf{p}) + \sum_{\ell=1}^7 \alpha_\ell \nabla\varphi_\ell(\mathbf{p}) \quad (6)$$

and

$$\mathbf{H}(\mathbf{p}) = \mathbf{H}_\phi(\mathbf{p}) + \sum_{\ell=1}^7 \alpha_\ell \mathbf{H}_\ell, \quad (7)$$

where

$$\nabla\phi(\mathbf{p}) = -\frac{2}{N} \mathbf{G}(\mathbf{p})^\top [\mathbf{d}^o - \mathbf{d}(\mathbf{p})] \quad (8)$$

and

$$\mathbf{H}_\phi(\mathbf{p}) = \frac{2}{N} \mathbf{G}(\mathbf{p})^\top \mathbf{G}(\mathbf{p}) \quad (9)$$

are the gradient vector of the Hessian matrix of the misfit function  $\phi(\mathbf{p})$  (eq. 5), respectively, the terms  $\nabla\varphi_\ell(\mathbf{p})$  and  $\mathbf{H}_\ell$ ,  $\ell = 1, \dots, 7$ , are the gradient vectors and Hessian matrices of the constraint functions, respectively, and  $\mathbf{G}(\mathbf{p})$  is an  $N \times M$  matrix whose element  $ij$  is the derivative of the predicted data  $d_i(\mathbf{p})$  (eq. 2) with respect to the  $j$  element  $p_j$  of the parameter vector  $\mathbf{p}$  (eq. 1). Details about the constraint functions  $\varphi_\ell(\mathbf{p})$ ,  $\ell = 1, \dots, 7$ , as well as the numerical procedure to solve this nonlinear inverse problem are given in the following sections.

### 2.3 Constraint functions

We have divided the constraint functions  $\varphi_\ell(\mathbf{p})$  (eq. 3),  $\ell = 1, \dots, 7$ , used here to obtain stable solutions and introduce prior information about the magnetic source into the following three groups.

### 2.3.1 Smoothness constraints

This group is formed by variations of the first-order Tikhonov regularization (Aster et al. 2019, p. 103) that imposes smoothness on the radii  $r_j^k$  and the Cartesian coordinates  $x_0^k$  and  $y_0^k$  of the origin  $O^k$ ,  $j = 1, \dots, V$ ,  $k = 1, \dots, L$ , defining the horizontal section of each prism (Fig.1b). They were proposed by Oliveira Jr. et al. (2011) and Oliveira Jr. & Barbosa (2013) and play a very important role in introducing prior information about the shape of the source.

The first constraint of this group is the *smoothness constraint on the adjacent radii defining the horizontal section of each vertical prism*. This constraint imposes that adjacent radii  $r_j^k$  and  $r_{j+1}^k$  within each prism must be close to each other. It forces the estimated prism to be approximately cylindrical. Mathematically, the constraint is given by

$$\begin{aligned}\varphi_1(\mathbf{p}) &= \sum_{k=1}^L \left[ (r_V^k - r_1^k)^2 + \sum_{j=1}^{V-1} (r_j^k - r_{j+1}^k)^2 \right] \\ &= \mathbf{p}^\top \mathbf{R}_1^\top \mathbf{R}_1 \mathbf{p} ,\end{aligned}\quad (10)$$

where

$$\mathbf{R}_1 = \mathbf{I}_L \otimes \begin{bmatrix} (\mathbf{I}_V - \mathbf{D}_V^\top) & \mathbf{0}_{V \times 2} \end{bmatrix}_{(L-1)V \times M} , \quad (11)$$

$\mathbf{I}_L$  is the identity matrix of order  $L$ , “ $\otimes$ ” denotes the Kronecker product (Horn & Johnson 1991, p. 243),  $\mathbf{0}_{V \times 2}$  is a  $V \times 2$  matrix with null elements,  $\mathbf{I}_V$  is the identity matrix of order  $V$  and  $\mathbf{D}_V^\top$  is the upshift permutation matrix of order  $V$  (Golub & Loan 2013, p. 20). The gradient and Hessian of function  $\varphi_1(\mathbf{p})$  (eq. 10) are given by:

$$\nabla \varphi_1(\mathbf{p}) = 2\mathbf{R}_1^\top \mathbf{R}_1 \mathbf{p} , \quad (12)$$

and

$$\mathbf{H}_1(\mathbf{p}) = 2\mathbf{R}_1^\top \mathbf{R}_1 . \quad (13)$$

The second constraint of this group is the *smoothness constraint on the adjacent radii of the vertically adjacent prisms*, which imposes that adjacent radii  $r_j^k$  and  $r_j^{k+1}$  within vertically adjacent prisms must be close to each other. This constraint forces the shape of all prisms to be similar to each other and is given by

$$\begin{aligned}\varphi_2(\mathbf{p}) &= \sum_{k=1}^{L-1} \left[ \sum_{j=1}^V (r_j^{k+1} - r_j^k)^2 \right] \\ &= \mathbf{p}^\top \mathbf{R}_2^\top \mathbf{R}_2 \mathbf{p}\end{aligned}\quad (14)$$

where

$$\mathbf{R}_2 = \begin{bmatrix} \mathbf{S}_2 & \mathbf{0}_{(L-1)V \times 1} \end{bmatrix}_{(L-1)V \times M}, \quad (15)$$

$$\mathbf{S}_2 = \left( \begin{bmatrix} \mathbf{I}_{L-1} & \mathbf{0}_{(L-1) \times 1} \end{bmatrix} - \begin{bmatrix} \mathbf{0}_{(L-1) \times 1} & \mathbf{I}_{L-1} \end{bmatrix} \right) \otimes \begin{bmatrix} \mathbf{I}_V & \mathbf{0}_{V \times 2} \end{bmatrix}, \quad (16)$$

$\mathbf{0}_{(L-1)V \times 1}$  is an  $(L-1)V \times 1$  vector with null elements,  $\mathbf{0}_{(L-1) \times 1}$  is an  $(L-1) \times 1$  vector with null elements and  $\mathbf{I}_{L-1}$  is the identity matrix of order  $L-1$ . The gradient and Hessian of function  $\varphi_2(\mathbf{p})$  (eq. 14) are given by:

$$\nabla \varphi_2(\mathbf{p}) = 2\mathbf{R}_2^\top \mathbf{R}_2 \mathbf{p}, \quad (17)$$

and

$$\mathbf{H}_2(\mathbf{p}) = 2\mathbf{R}_2^\top \mathbf{R}_2. \quad (18)$$

The last constraint of this group is the *smoothness constraint on the horizontal position of the arbitrary origins of the vertically adjacent prisms*. This constraint imposes that the estimated horizontal Cartesian coordinates  $(x_0^k, y_0^k)$  and  $(x_0^{k+1}, y_0^{k+1})$  of the origins  $O^k$  and  $O^{k+1}$  of adjacent prisms must be close to each other. It forces the centers of the prisms to be vertically aligned. This constraint is given by

$$\begin{aligned} \varphi_3(\mathbf{p}) &= \sum_{k=1}^{L-1} \left[ (x_0^{k+1} - x_0^k)^2 + (y_0^{k+1} - y_0^k)^2 \right], \\ &= \mathbf{p}^\top \mathbf{R}_3^\top \mathbf{R}_3 \mathbf{p} \end{aligned} \quad (19)$$

where

$$\mathbf{R}_3 = \begin{bmatrix} \mathbf{S}_3 & \mathbf{0}_{(L-1)2 \times 1} \end{bmatrix}_{(L-1)2 \times M}, \quad (20)$$

$$\mathbf{S}_3 = \left( \begin{bmatrix} \mathbf{I}_{L-1} & \mathbf{0}_{(L-1) \times 1} \end{bmatrix} - \begin{bmatrix} \mathbf{0}_{(L-1) \times 1} & \mathbf{I}_{L-1} \end{bmatrix} \right) \otimes \begin{bmatrix} \mathbf{0}_{2 \times V} & \mathbf{I}_2 \end{bmatrix}, \quad (21)$$

$\mathbf{0}_{(L-1)2 \times 1}$  is an  $(L-1)2 \times 1$  vector with null elements,  $\mathbf{0}_{2 \times V}$  is a  $2 \times V$  matrix with null elements and  $\mathbf{I}_2$  is the identity matrix of order 2. The gradient and Hessian of function  $\varphi_3(\mathbf{p})$  (eq. 19) are given by:

$$\nabla \varphi_3(\mathbf{p}) = 2\mathbf{R}_3^\top \mathbf{R}_3 \mathbf{p}, \quad (22)$$

and

$$\mathbf{H}_3(\mathbf{p}) = 2\mathbf{R}_3^\top \mathbf{R}_3. \quad (23)$$

### 2.3.2 Equality constraints

This group is formed by two constraints that were proposed by Oliveira Jr. et al. (2011) and Oliveira Jr. & Barbosa (2013) by following the same approach proposed Barbosa et al. (1997) and Barbosa

et al. (1999a). They introduce a priori information about the shallowest prism and are suitable for outcropping sources.

The *source's outcrop constraint* imposes that the horizontal cross-section of the shallowest prism must be close to known outcropping boundary of the geologic source. Mathematically, this constraint is given by

$$\begin{aligned}\varphi_4(\mathbf{p}) &= \left[ (x_0^1 - x_0^0)^2 + (y_0^1 - y_0^0)^2 + \sum_{j=1}^V (r_j^1 - r_j^0)^2 \right] , \\ &= (\mathbf{R}_4 \mathbf{p} - \mathbf{a})^\top (\mathbf{R}_4 \mathbf{p} - \mathbf{a})\end{aligned}\quad (24)$$

where  $\mathbf{a}$  is a  $V + 2 \times 1$  vector containing the radii and the horizontal Cartesian coordinates of the polygon defining the outcropping boundary

$$\mathbf{a} = \begin{bmatrix} \tilde{r}_1^0 & \dots & \tilde{r}_V^0 & \tilde{x}_0^0 & \tilde{y}_0^0 \end{bmatrix}^\top , \quad (25)$$

and

$$\mathbf{R}_4 = \begin{bmatrix} \mathbf{I}_{V+2} & \mathbf{0}_{(V+2) \times (M-V-2)} \end{bmatrix}_{(V+2) \times M} , \quad (26)$$

where  $\mathbf{I}_{V+2}$  is the identity matrix of order  $V + 2$  and  $\mathbf{0}_{(V+2) \times (M-V-2)}$  is a matrix with null elements. The gradient and Hessian of function  $\varphi_4(\mathbf{p})$  (eq. 24) are given by:

$$\nabla \varphi_4(\mathbf{p}) = 2\mathbf{R}_4^\top (\mathbf{R}_4 \mathbf{p} - \mathbf{a}) , \quad (27)$$

and

$$\mathbf{H}_4(\mathbf{p}) = 2\mathbf{R}_4^\top \mathbf{R}_4 . \quad (28)$$

The *source's horizontal location constraint* imposes that the horizontal Cartesian coordinates of the origin within the shallowest prism must be as close as possible to a known outcropping point. This constraint is given by

$$\begin{aligned}\varphi_5(\mathbf{p}) &= \left[ (x_0^1 - x_0^0)^2 + (y_0^1 - y_0^0)^2 \right] , \\ &= (\mathbf{R}_5 \mathbf{p} - \mathbf{b})^\top (\mathbf{R}_5 \mathbf{p} - \mathbf{b})\end{aligned}\quad (29)$$

where  $\mathbf{b}$  is a  $2 \times 1$  vector containing the horizontal Cartesian coordinates of the outcropping point

$$\mathbf{b} = \begin{bmatrix} \tilde{x}_0^0 & \tilde{y}_0^0 \end{bmatrix}^\top , \quad (30)$$

and

$$\mathbf{R}_5 = \begin{bmatrix} \mathbf{0}_{2 \times V} & \mathbf{I}_2 & \mathbf{0}_{2 \times (M-V-2)} \end{bmatrix}_{2 \times M} , \quad (31)$$

where  $\mathbf{I}_2$  is the identity matrix of order 2 and  $\mathbf{0}_{2 \times (M-V-2)}$  and  $\mathbf{0}_{2 \times V}$  are matrices with null elements.

The gradient and Hessian of function  $\varphi_5(\mathbf{p})$  (eq. 29) are given by:

$$\nabla \varphi_5(\mathbf{p}) = 2\mathbf{R}_5^T (\mathbf{R}_5 \mathbf{p} - \mathbf{b}) , \quad (32)$$

and

$$\mathbf{H}_5(\mathbf{p}) = 2\mathbf{R}_5^T \mathbf{R}_5 . \quad (33)$$

### 2.3.3 Minimum Euclidean norm constraints

Two constraints use the zeroth-order Tikhonov regularization with the purpose of obtaining stable solutions without necessarily introducing significant a priori information about the source.

The *Minimum Euclidean norm of the radii* imposes that all estimated radii within each prism must be close to null values. This constraint was proposed by Oliveira Jr. et al. (2011) and Oliveira Jr. & Barbosa (2013) and can be rewritten as follows

$$\begin{aligned} \varphi_6(\mathbf{p}) &= \sum_{k=1}^L \sum_{j=1}^V \left( r_j^k \right)^2 , \\ &= \mathbf{p}^T \mathbf{R}_6^T \mathbf{R}_6 \mathbf{p} \end{aligned} \quad (34)$$

where

$$\mathbf{R}_6 = \begin{bmatrix} \mathbf{S}_6 & \mathbf{0}_{(M-1) \times 1} \\ \mathbf{0}_{1 \times (M-1)} & 0 \end{bmatrix}_{M \times M} , \quad (35)$$

and

$$\mathbf{S}_6 = \begin{bmatrix} \mathbf{I}_V & \mathbf{0}_{V \times 2} \\ \mathbf{0}_{2 \times V} & \mathbf{I}_2 \end{bmatrix}_{(V+2) \times (V+2)} . \quad (36)$$

The gradient and Hessian of function  $\varphi_6(\mathbf{p})$  (eq. 34) are given by:

$$\nabla \varphi_6(\mathbf{p}) = 2\mathbf{R}_6^T \mathbf{R}_6 \mathbf{p} , \quad (37)$$

and

$$\mathbf{H}_6(\mathbf{p}) = 2\mathbf{R}_6^T \mathbf{R}_6 . \quad (38)$$

The other constraint, the *Minimum Euclidean norm of the prism thickness*, imposes that the thickness of all prisms must be close to zero. We present this constraint to introduce a priori information about the maximum depth of the source. It is given by

$$\begin{aligned} \varphi_7(\mathbf{p}) &= dz^2 , \\ &= \mathbf{p}^T \mathbf{R}_7^T \mathbf{R}_7 \mathbf{p} \end{aligned} \quad (39)$$

where

$$\mathbf{R}_7 = \begin{bmatrix} \mathbf{0}_{(M-1) \times (M-1)} & \mathbf{0}_{(M-1) \times 1} \\ \mathbf{0}_{1 \times (M-1)} & 1 \end{bmatrix}_{M \times M}. \quad (40)$$

The gradient and Hessian of function  $\varphi_7(\mathbf{p})$  (eq. 39) are given by:

$$\nabla \varphi_7(\mathbf{p}) = 2\mathbf{R}_7^T \mathbf{R}_7 \mathbf{p} \quad , \quad (41)$$

and

$$\mathbf{H}_7(\mathbf{p}) = 2\mathbf{R}_7^T \mathbf{R}_7 \quad . \quad (42)$$

## 2.4 Computational procedures

To estimate the parameter vector  $\mathbf{p}$  (eq. 1) that minimizes the goal function  $\Gamma(\mathbf{p})$  (eq. 3), subject to the inequality constraint (eq. 4), we use the Levenberg-Marquardt method (e.g., Aster et al. 2019, p. 240). This is an iterative gradient-based method that, at each iteration  $k$ , updates the estimate parameter vector  $\hat{\mathbf{p}}_{(k)}$  (where the superscript hat “ $\hat{\cdot}$ ” denotes estimated) to obtain a new estimated parameter vector  $\hat{\mathbf{p}}_{(k+1)}$ . We compute this update by following the same strategy of Barbosa et al. (1999b), Oliveira Jr. et al. (2011) and Oliveira Jr. & Barbosa (2013) to incorporate the inequality constraint (eq. 4). This strategy consists in transforming each element  $\hat{p}_l$  of the estimated parameter vector  $\hat{\mathbf{p}}_{(k)}$  into the element  $\hat{p}_l^\dagger$  of a new vector  $\hat{\mathbf{p}}_{(k)}^\dagger$  as follows:

$$\hat{p}_l^\dagger = -\ln \left( \frac{p_l^{max} - \hat{p}_l}{\hat{p}_l - p_l^{min}} \right) \quad , \quad (43)$$

where  $p_l^{min}$  and  $p_l^{max}$  are defined in the inequality constraint (eq. 4). Then, we compute a correction  $\Delta \hat{\mathbf{p}}_{(k)}^\dagger$  and a new vector  $\hat{\mathbf{p}}_{(k+1)}^\dagger = \hat{\mathbf{p}}_{(k)}^\dagger + \Delta \hat{\mathbf{p}}_{(k)}^\dagger$ . Finally, we transform each element  $\hat{p}_l^\dagger$  of  $\hat{\mathbf{p}}_{(k+1)}^\dagger$  into the element  $\hat{p}_l$  of the new estimated parameter vector  $\hat{\mathbf{p}}_{(k+1)}$  as follows:

$$\hat{p}_l = p_l^{min} + \left( \frac{p_l^{max} - p_l^{min}}{1 + e^{-\hat{p}_l^\dagger}} \right) \quad . \quad (44)$$

### 2.4.1 Considerations about the weights $\alpha_1 - \alpha_7$

Attributing values to the weights  $\alpha_\ell$  (eq. 3) is an important feature of our method. However, there is no analytical rule to define them and their values can be dependent on the particular characteristics of the type of geological setting where the method is being applied Silva et al. (2001). To overcome this problem, we normalize the  $\alpha_\ell$  values as follows:

$$\alpha_\ell = \tilde{\alpha}_\ell \frac{E_\phi}{E_\ell}, \quad \ell = 1, \dots, 7, \quad (45)$$

where  $\tilde{\alpha}_\ell$  is a positive scalar and  $E_\phi/E_\ell$  is a normalizing factor. In this equation,  $E_\ell$  represents the trace of the Hessian matrix  $\mathbf{H}_\ell$  (eqs 13, 18, 23, 28, 33, 38, and 42) of the  $\ell$ th constraining function  $\varphi_\ell(\mathbf{p})$  (eqs 10, 14, 19, 24, 29, 34, and 39). The constant  $E_\phi$  is the trace of the Hessian matrix  $\mathbf{H}_\phi(\mathbf{p}_0)$  (eq. 9) of the misfit function  $\phi(\mathbf{p})$  (eq. 5) computed with the initial approximation  $\hat{\mathbf{p}}_{(0)}$  for the parameter vector  $\mathbf{p}$  (eq. 1) at the beginning of the inversion algorithm. According to this empirical strategy, the weights  $\alpha_\ell$  are defined using the positive scalars  $\tilde{\alpha}_\ell$  (eq. 45), which are less dependent on the particular characteristics of the interpretation geological setting.

#### 2.4.2 Inversion algorithm

At each iteration  $k$  of our algorithm, the correction  $\Delta\hat{\mathbf{p}}_{(k)}^\dagger$  is computed by solving the following linear system:

$$\mathbf{Q}_{(k)} \left[ \mathbf{Q}_{(k)} \mathbf{H}^\dagger(\hat{\mathbf{p}}_{(k)}) \mathbf{Q}_{(k)} + \lambda_{(k)} \mathbf{I} \right] \mathbf{Q}_{(k)} \Delta\hat{\mathbf{p}}_{(k)}^\dagger = -\nabla\Gamma(\hat{\mathbf{p}}_{(k)}) , \quad (46)$$

where  $\lambda_{(k)}$  is a positive scalar (known as Marquardt parameter) which is adjusted at each iteration and is associated with the Levenberg-Marquardt method (e.g., Silva et al. 2001; Aster et al. 2019, p. 240),  $\mathbf{I}$  is the identity matrix with order  $M$ ,  $\nabla\Gamma(\hat{\mathbf{p}})$  is the gradient of the goal function (eq. 6) and  $\mathbf{H}^\dagger(\hat{\mathbf{p}}_{(k)})$  is a matrix given by

$$\mathbf{H}^\dagger(\hat{\mathbf{p}}_{(k)}) = \mathbf{H}(\hat{\mathbf{p}}_{(k)}) \mathbf{T}(\hat{\mathbf{p}}_{(k)}) , \quad (47)$$

where  $\mathbf{H}(\hat{\mathbf{p}}_{(k)})$  is the Hessian matrix of the goal function (eq. 7) and  $\mathbf{T}(\hat{\mathbf{p}}_{(k)})$  is a diagonal matrix whose element  $ll$  is given by

$$t(\hat{p}_l) = \frac{(p_l^{max} - \hat{p}_l)(\hat{p}_l - p_l^{min})}{p_l^{max} - p_l^{min}}, \quad l = 1, \dots, M , \quad (48)$$

with  $p_l$  being the  $l$ th element of the estimated parameter vector  $\hat{\mathbf{p}}_{(k)}$ . In eq. 46,  $\mathbf{D}_{(k)}$  is a diagonal matrix proposed by Marquardt (1963) for scaling the parameter  $\lambda_{(k)}$  at each iteration and improving the convergence of the algorithm. The element  $ll$  of this diagonal matrix is given by

$$q_{ll} = \frac{1}{\sqrt{h_{ll}^\dagger}} , \quad (49)$$

where  $h_{ll}^\dagger$  is the element  $ll$  of the matrix  $\mathbf{H}^\dagger(\hat{\mathbf{p}}_{(k)})$  (eq. 47).

#### 2.4.3 Practical considerations

Our algorithm depends on several variables that significantly impact the estimated models and cannot be automatically set without the interpreter's judgment. They are the  $\tilde{\alpha}_1 - \tilde{\alpha}_7$  (eq. 45). Based on our practical experience, we suggest some empirical procedures for setting these parameters.

The parameters  $\tilde{\alpha}_1$  and  $\tilde{\alpha}_2$  impose prior information on the shape of the horizontal cross-section

of the prisms. The first one forces all prisms to have a circular horizontal cross-section, while the second forces all prisms to have a similar horizontal cross-section. Generally, their values vary from  $10^{-5}$  to  $10^{-3}$  and differs from each other by one order of magnitude, at most. The parameter  $\tilde{\alpha}_3$  also varies from  $10^{-5}$  to  $10^{-3}$  and controls the relative position of adjacent prisms forming the model. A high value privileges a vertical estimated body, whereas a small value tends to generate an inclined estimated body.

In comparison to  $\tilde{\alpha}_1$ ,  $\tilde{\alpha}_2$  and  $\tilde{\alpha}_3$ , the other parameters usually have smaller values varying from  $10^{-7}$  to  $10^{-5}$ . The parameters  $\tilde{\alpha}_4$  and  $\tilde{\alpha}_5$  are used when a priori information about the source is available at the study area. The parameter  $\tilde{\alpha}_6$  has a purely mathematical meaning and it is used only to obtain stable solutions for the inverse problem. Its value is set to be as small as possible. The parameter  $\tilde{\alpha}_7$  controls the total-vertical extension of the the estimated body. The greater its value, the shallower the estimated depth to the bottom of the source will be and vice versa. A general rule is starting with values  $\tilde{\alpha}_1 = 10^{-4}$ ,  $\tilde{\alpha}_2 = 10^{-4}$ ,  $\tilde{\alpha}_3 = 10^{-4}$ ,  $\tilde{\alpha}_4 = 0$ ,  $\tilde{\alpha}_5 = 0$ ,  $\tilde{\alpha}_6 = 10^{-7}$ ,  $\tilde{\alpha}_7 = 10^{-5}$  and change them to refine the results.

Another important aspect of our method is the initial approximation  $\hat{\mathbf{p}}_{(0)}$ . We set the same constant radii for all prisms, simulating a cylindrical source located below the positive and negative parts of the observed anomaly. Also, we set the same constant thickness  $dz$  for all prisms with the purpose of generating a bottom depth greater than that we expect for the true source. Finally, we adjust the parameters of the initial approximation  $\hat{\mathbf{p}}_{(0)}$  in order to obtain a preliminary fit of the observed data.

### 3 APPLICATION TO SYNTHETIC DATA

#### 3.1 Simple model test

We have simulated a lopolithic intrusion, a funnel-shaped source (Cawthorn & Miller 2018), with simple geometry (blue prisms in Figs 3b and 5), which extends from  $z_0 = 0$  m to 1 600 m along depth and satisfies most of the constraints described in subsection 2.3. It is formed by  $L = 8$  prisms, all of them with the same number of vertices  $V = 20$ , thickness  $dz = 200$  m and horizontal coordinates  $(x_0^k, y_0^k) = (0, 0)$  m of the origins  $O^k$ ,  $k = 1, \dots, L$ . The radii of all vertices are equal to each other within the same prism and decrease linearly with depth, varying from  $r_j^0 = 1920$  m, at the shallowest prism,  $r_j^L = 800$  m, at the deepest prism,  $j = 1, \dots, V$ . All prisms have the same total-magnetization direction with inclination  $-21.5^\circ$ , declination  $-18.7^\circ$  and intensity  $m_0 = 9$  A/m. We calculated the total-field anomaly produced by this simple model, in an area of  $100 \text{ km}^2$  area, by simulating an airborne survey composed of 21 flight lines that are equally spaced 500 m apart along the  $y$  axis, at a constant vertical coordinate  $z = -150$  m. At each line, there are 100 observation points spaced 101 m apart along  $x$  axis. The total-field anomaly is corrupted with a pseudorandom Gaussian noise having mean  $\mu_0 = 0$  nT and standard deviation  $\sigma_0 = 5$  nT (Fig. 3a).

We have inverted the noise-corrupted total-field anomaly (Fig. 3a) produced by the simulated lopolith-like body (blue prisms in Fig. 3b) and obtained 36 different estimates. Each estimate was obtained by using different pairs of depth to the top  $z_0$  and total-magnetization intensity  $m_0$  (Fig. 4). All estimates were generated by using the true values of total-magnetization inclination and declination, the same interpretation model formed by  $L = 5$  prisms, each one with  $V = 20$  vertices, and the same weights for the constraining functions:  $\tilde{\alpha}_1 = 10^{-5}$ ,  $\tilde{\alpha}_2 = 10^{-4}$ ,  $\tilde{\alpha}_3 = 10^{-4}$ ,  $\tilde{\alpha}_4 = 0$ ,  $\tilde{\alpha}_5 = 0$ ,  $\tilde{\alpha}_6 = 10^{-7}$ , and  $\tilde{\alpha}_7 = 10^{-6}$ . In all inversions, the initial approximation for  $\hat{\mathbf{p}}_{(0)}$  has the same constant radii  $r_j^k = 2000$  m,  $k = 1, \dots, L$ ,  $j = 1, \dots, V$ , the same prism's thicknesses  $dz = 350$  m and the same origins  $(x_0^k, y_0^k) = (0, 0)$  m for all prisms.

Fig. 4 shows the discrete mapping of the goal functional  $\Gamma(\mathbf{p})$  (eq. 3) on the plane of the total-magnetization intensity ( $m_0$ ) versus depth to the top ( $z_0$ ). The true values of depth to the top  $z_0$  and total-magnetization intensity  $m_0$  (represented by the red triangle in Fig. 4) produces the smallest value of goal function  $\Gamma(\mathbf{p})$  (eq. 3). Fig. 5a shows that this estimated model (red prisms in Figs 5c and d) not only fits the noise-corrupted data, but also retrieves the geometry of the true model (blue prisms). The inset in Fig. 5a shows that the residuals follow a normal distribution with mean  $\mu$  and standard deviation  $\sigma$  compatible with those values used to generate the synthetic noise. The estimated thickness of each prism is  $dz = 297.65$  m resulting in a depth-to-bottom estimate (1 485 m) very close to the true one (1 600 m). These results illustrate the good performance of our method in an ideal case.

### 3.2 Complex model test

We have simulated a complex inclined body (blue prisms in Figs 6 and 8) inspired by an alkaline vertical dipping intrusion. The simulated intrusion extends from  $z_0 = 130$  m to 5270 m along depth and violates most of the constraints described in subsection 2.3. It is formed by  $L = 10$  prisms, all of them with the same number of vertices  $V = 30$  of thickness  $dz = 600$  m. The horizontal coordinates of the origins  $O^k$  vary linearly from  $(x_0^0, y_0^0) = (-250, 750)$  m, at the shallowest prism, to  $(x_L^0, y_L^0) = (250, -750)$  m resulting a dip in the direction NW-SE, at the deepest prism. The displacements of the horizontal coordinates of the origins  $O_k$  resulted in a simulated source dipping to northwest (blue prisms in Figs 6 and 8). The radii  $r_j^k, k = 1, \dots, L, j = 1, \dots, V$ , defining the vertices vary from 240 m to 1540 m and also differ from each other within the same prism. All prisms have a constant total magnetization with inclination  $-50^\circ$ , declination  $9^\circ$  and intensity  $m_0 = 12$  A/m. We are simulating an alkaline vertical dipping intrusion. We have calculated the total-field anomaly produced by this complex model, in an area of  $100 \text{ km}^2$ , by simulating an airborne survey composed of 18 north-south flight lines distributed from  $-5000$  m to  $5000$  m along the  $y$  axis and a single east-west tie line approximately located at  $x = 0$  m. The data points are located on the undulated surface shown in Fig. 6a. Notice that both flight and tie lines are not perfectly straight. To compute the synthetic total-field anomaly, we consider a constant main field with inclination  $-21.5^\circ$  and declination  $-18.7^\circ$ , which is significantly different from the total-magnetization direction of the complex model. Finally, we have contaminated the synthetic total-field anomaly with a pseudorandom Gaussian noise having mean and standard deviation equal to 0 nT and 5 nT, respectively (Fig. 6a).

We have inverted the noise-corrupted total-field anomaly (Fig. 6a) produced by the complex model by using 36 different pairs of depth to the top  $z_0$  and total-magnetization intensity  $m_0$  (Fig. 7). Differently from the previous simulation with a simple model, the present generated grid of  $m_0$  and  $z_0$  does not contain the true ones (represented by the red triangle in Fig. 7). All models were generated by using the true direction of the main geomagnetic field (i.e., inclination  $-21.5^\circ$  and declination  $-18.7^\circ$ ), the same interpretation model formed by  $L = 8$  prisms, each one with  $V = 20$  vertices, and the same weights for the constraining functions:  $\tilde{\alpha}_1 = 10^{-5}, \tilde{\alpha}_2 = 10^{-4}, \tilde{\alpha}_3 = 10^{-4}, \tilde{\alpha}_4 = 0, \tilde{\alpha}_5 = 0, \tilde{\alpha}_6 = 10^{-7}$ , and  $\tilde{\alpha}_7 = 10^{-5}$ . The initial approximation  $\hat{\mathbf{p}}_{(0)}$  for all inversions has the same constant radii  $r_j^k = 800$  m,  $k = 1, \dots, L, j = 1, \dots, V$ , the same thickness  $dz = 650$  m and the same origin  $(x_0^k, y_0^k) = (-300, 300)$  m for all prisms.

Fig. 7 shows the goal function  $\Gamma(\mathbf{p})$  (eq. 3), with different total-magnetization intensity  $m_0$  and depth-to-the-top  $z_0$  on the plane  $(m_0 \times z_0)$ . We note that a minimum region (dark blue region in Fig. 7) contains the true pair of  $m_0$  and  $z_0$  (red triangle in Fig. 7). However, we do not use the true  $m_0$  and  $z_0$  to retrieve the magnetized source because, intentionally in this test, our coarse mapping of the

goal function  $\Gamma(\mathbf{p})$  does not include them. Nevertheless, a well-defined minimum of the goal function value (pinpointed as the cyan diamond in Fig. 7) is achieved when the total-magnetization intensity  $m_0 = 11.4 \text{ A/m}$  and depth to the top at  $z_0 = 150 \text{ m}$  with different total-magnetization intensity  $m_0$  and depth-to-the-top  $z_0$  on the plane ( $m_0 \times z_0$ ). We note that a minimum region (dark blue region in Fig. 7) contains the true pair of  $m_0$  and  $z_0$  (red triangle in Fig. 7). However, we do not use the true  $m_0$  and  $z_0$  to retrieve the magnetized source because, intentionally in this test, our coarse mapping of the goal function  $\Gamma(\mathbf{p})$  does not include them. Nevertheless, a well-defined minimum of the goal function value (pinpointed as the white diamond in Fig. 7) is achieved when the total-magnetization intensity  $m_0 = 11.4 \text{ A/m}$  and depth to the top at  $z_0 = 150 \text{ m}$ . These values of  $m_0$  and  $z_0$  will be used to retrieve the estimated model.

Fig. 8 shows that the estimated model (red prisms in Figs 8c and d) fits the noise-corrupted data and also retrieves the geometry of the true source (blue prisms). Note that the red prisms edges accurately matches the blue prisms ones. The inset in Fig. 5a shows that the residuals follow a normal distribution with mean  $\mu$  and standard deviation  $\sigma$  compatible with those values used to generate the noise-corrupted data. The estimated of depth to the bottom (5 662.2 m) and volume (11.56 km<sup>3</sup>) are underestimated, but still close to the true values (5 570 m and 12.60 km<sup>3</sup>). These results show that our method can also be very useful to interpret complex sources, even if they do not perfectly satisfy the constraints imposed to solve the nonlinear inverse problem.

#### 4 APPLICATION TO FIELD DATA

We have applied our method to interpret airborne magnetic data provided by Geological Survey of Brazil (CPRM) over the Anitápolis complex, in southern Brazil. The airborne survey was flown with north-south and east-west lines spaced by 500 m and 10 000 m from each other, respectively. The total-field anomaly data were corrected from daytime variation and subtracted from the main geomagnetic field using the IGRF. The inclination, declination and intensity of the main geomagnetic field at the study area, for the period of the survey, are  $-37.05^\circ$ ,  $-18.17^\circ$  and  $\approx 22\,768$  nT, respectively. To isolate the target total-field anomaly, we have applied a regional separation using a second-order polynomial fit resulting in the residual data shown in Fig. 9a. Fig. 9b and 9c show the geometric height (referred to the WGS84 ellipsoid) and UTM horizontal coordinates of the data and the topography, respectively. For convenience, we have subtracted 800 m from the height values.

The Anitápolis alkaline-carbonatitic complex forms a circular concentric body ( $\approx 6$  km $^2$  in area) containing magnetite as part of its mineralogical composition. It intruded into the Late Proterozoic leucogranites of the Dom Feliciano mobile belt in the Early Cretaceous (132 Ma), apparently concomitant with the voluminous flood tholeiitic basalts of the Serra Geral Formation (133-130 Ma) at the southern side of the Paraná Basin (Gibson et al. 1999; Scheibe et al. 2005). As pointed out by Gomes et al. (2018), there is still some debate about the emplacement of the Anitápolis alkaline-carbonatitic complex. Melcher & Coutinho (1966) pointed out the influence of N-S-trending faults. Scheibe et al. (2005) considered that it is roughly emplaced along the E-W Rio Uruguay Lineament. According to Riccomini et al. (2005), the Anitápolis complex does not show a clear structural control.

We set the total-magnetization direction of the interpretation model with inclination  $I = -21^\circ$  and declination  $D = -11^\circ$ . These values were estimated by Reis et al. (2019) for the study area by using a method based on the equivalent-layer technique (Dampney 1969; Emilia 1973). We have verified this estimated direction using the reduction to the pole technique (not shown). This total-magnetization direction indicates the presence of remanent magnetization. Laboratory measurements on rock samples obtained at the Jacupiranga complex, another alkaline complex located northward of the study area, with the same age as the Anitápolis complex, show total-magnetization intensities values varying from approximately 0.01 to 29.90 A/m (Alva-Valdivia et al. 2009, tb. 1). We used these values as a priori information to constraint the total-magnetization intensity  $m_0$  of the Anitápolis complex.

We used an interpretation model formed by  $L = 6$  prisms, each one with  $V = 20$  vertices defining their horizontal cross-sections. We inverted the observed total-field anomaly (Fig. 9a) for each pair of  $m_0$  and  $z_0$  shown in Fig. 10, resulting in 100 estimated models. For all models, we set an initial approximation  $\hat{\mathbf{p}}_{(0)}$  with origin at  $(x_0^k, y_0^k) = (6921, 688)$  km, constant radii  $r_j^k = 700$  m for all

vertices forming all prisms and the same constant thickness  $dz = 900$  m. We also set the same weights which were used in the synthetic tests, i.e.,  $\tilde{\alpha}_1 = 10^{-4}$ ,  $\tilde{\alpha}_2 = 10^{-3}$ ,  $\tilde{\alpha}_3 = 10^{-4}$ ,  $\tilde{\alpha}_4 = 0$ ,  $\tilde{\alpha}_5 = 0$ ,  $\tilde{\alpha}_6 = 10^{-8}$ , and  $\tilde{\alpha}_7 = 10^{-5}$  (eq. 45).

Fig. 10 shows that, similarly to the previous synthetic test with the complex model (Fig. 7), there is a region containing candidate solutions producing small values for the goal function  $\Gamma(\mathbf{p})$  (eq. 3), with different values of  $m_0$  and  $z_0$ . The pink diamond in Fig. 10 represents the estimated model shown in Fig. 11. This model produces the smallest value for  $\Gamma(\mathbf{p})$  (3), it has a volume  $9.96 \text{ km}^3$ , total thickness of  $4596.55$  m ( $dz = 766.10$ ), depth-to-the-top  $z_0 = 20$  m and total-magnetization intensity  $m_0 = 14.0 \text{ A/m}$ . Fig. 12a shows that this estimated model produces a reasonable data fit. This estimated depth-to-the-top  $z_0$  indicates a non-outcropping source, which is compatible with a priori information about the study area. We do not have evidences of an outcropping source for this anomaly, although there are outcropping intrusions in the area of the Anitápolis complex (Gibson et al. 1999). The estimated total-magnetization intensity  $m_0$  is also compatible with the available a priori information. It is within the range found by Alva-Valdivia et al. (2009) in the Jacupiranga complex.

The white diamond in Fig. 10 represents the alternative model shown in Fig. 12. This model is similar to that shown in Fig. 11. It has a volume  $9.57 \text{ km}^3$ , total thickness  $4419.34$  m ( $dz = 736.56$ ), depth-to-the-top  $z_0 = 0$  m and total-magnetization intensity  $m_0 = 14 \text{ A/m}$ . In comparison with the estimated model shown in Fig. 11, the alternative model shown in Fig. 12 has a shallower top and a very similar geometry. Both estimated models show a northwest-southeast elongated body with accentuated dip along depth (Figs 11 and 12). This is the same direction associated with the Serra Geral Lineament, crossing the study area, the Ponta Grossa Arch and the Torres syncline, which are prominent structural features located, respectively, northward and southward of the study area (e.g., Scheibe et al. 2005, p. 535). The total-magnetization intensities and depths-to-the-top estimates are compatible with the available a priori information and produce reasonable data fits. Hence, both models represent the possible geometry of the Anitápolis complex.

## 5 CONCLUSIONS

We have developed a total-field anomaly nonlinear inversion to estimate the shape of an isolated 3-D geological body assuming the knowledge about its total-magnetization direction. We approximate the body by a set of vertically stacked right prisms. The horizontal cross-section of each prism is a polygon defined by a given number of equally spaced vertices from  $0^\circ$  to  $360^\circ$ . We performed our inversion for a set of given depths to the top and total-magnetization intensities these results illustrate the inherent ambiguity of potential-field methods in retrieving both the physical-property distribution and volume of the sources. In this case, some a priori information must be used to constraint the range of reliable solutions. For each depth to the top and total-magnetization intensity, our method estimates the geometry of the cross-sections (the radii associated with the polygon vertices), the thickness and the horizontal position of the prisms. The estimated model approximates the 3-D geological body by solving a constrained nonlinear magnetic inversion. The estimated bodies producing the smallest values of the goal function form the set of candidate solutions that yields an acceptable data fitting satisfying stabilizing functions. To obtain stable solutions, we introduce a set of seven constraints on the source shape. Our method is an extension of previous works developed for retrieving the geometry of 3-D bodies by inverting gravity and gravity-gradient data. We not only adapted the previous methods for interpreting total-field anomaly data, but also generalize them to include the depth to the top and depth extension of the prisms among the estimated parameters.

Applications to synthetic data produced by a simple symmetric source illustrate the efficiency of our method in an ideal case. Moreover, the results obtained with synthetic data produced by a complex source, with variable dip and shape along depth, show that our method can also be used to interpret magnetic data produced by a realistic geological source. Both tests with synthetic data show that our method is able to retrieve the source's shape and fit the data.

We applied our method to interpret a total-field anomaly data over the alkaline-carbonatitic complex of Anitápolis, in southern Brazil. We obtained two candidate models having similar shapes, depths to the top and total-magnetic intensities, all of them in close agreement with the available a priori information. Both estimated models suggest that the emplacement of the Anitápolis complex seems to be controlled by northwest-southeast-trending faults at depth. This is the same direction associated with the Serra Geral Lineament, crossing the study area, and the prominent structural features Ponta Grossa Arch and Torres syncline, which are located northward and southward of the study area, respectively. Possible extensions of this work is the inversion of elongated and/or multiple sources. In addition, an the combination of gradient-based and heuristic optimization methods could be applied to estimate optimal regularization weights, overcoming problems with local minima.

## ACKNOWLEDGMENTS

## REFERENCES

- Abedi, M., Asghari, O., & Norouzi, G.-H., 2015. Collocated cokriging of iron deposit based on a model of magnetic susceptibility: a case study in Morvarid mine, Iran, *Arabian Journal of Geosciences*, **8**(4), 2179–2189.
- Alva-Valdivia, L. M., Perrin, M., Rivas-Sánchez, M. L., Goguitchaichvili, A., López-Loera, H., Lopes, O. F., & Bonás, T. B., 2009. Rock magnetism and microscopy of the jacupiranga alkaline-carbonatitic complex, southern brazil, *Earth, Planets and Space*, **61**(1), 161–171.
- Aster, R. C., Borchers, B., & Thurber, C. H., 2019. *Parameter Estimation and Inverse Problems*, Elsevier, 3rd edn.
- Ballantyne, E. J., 1980. Magnetic curve fit for a thin dike; calculator program (TI 59), *Geophysics*, **45**(3), 447–455.
- Barbosa, V. C. & Silva, J. B., 2006. Interactive 2d magnetic inversion: A tool for aiding forward modeling and testing geologic hypotheses, *Geophysics*, **71**(5), L43–L50.
- Barbosa, V. C. F., Silva, J. B. C., & Medeiros, W. E., 1997. Gravity inversion of basement relief using approximate equality constraints on depths, *Geophysics*, **62**, 1745–1757.
- Barbosa, V. C. F., Silva, J. B. C., & Medeiros, W. E., 1999a. Gravity inversion of a discontinuous relief stabilized by weighted smoothness constraints on depth, *Geophysics*, **64**(5), 1429–1437.
- Barbosa, V. C. F., Silva, J. B. C., & Medeiros, W. E., 1999b. Stable inversion of gravity anomalies of sedimentary basins with nonsmooth basement reliefs and arbitrary density contrast variations, *Geophysics*, **64**(3), 754–764.
- Bhattacharyya, B. K., 1980. A generalized multibody model for inversion of magnetic anomalies, *Geophysics*, **45**(2), 255–270.
- Caratori Tontini, F., Cocchi, L., & Carmisciano, C., 2006. Depth-to-the-bottom optimization for magnetic data inversion: Magnetic structure of the latium volcanic region, italy, *Journal of Geophysical Research*, **111**, B11104.
- Cawthorn, R. & Miller, J., 2018. Lopolith – A 100 year-old term. Is it still definitive?, *South African Journal of Geology*, **121**(3), 253–260.
- Cella, F. & Fedi, M., 2012. Inversion of potential field data using the structural index as weighting function rate decay: Inversion of potential field data, *Geophysical Prospecting*, **60**(2), 313–336.
- Cribb, J., 1976. Application Of The Generalized Linear Inverse To The Inversion Of Static Potential Data, *Geophysics*, **41**(6), 1365–1369.
- Dampney, C. N. G., 1969. The equivalent source technique, *Geophysics*, **34**(1), 39–53.
- Emilia, D. A., 1973. Equivalent sources used as an analytic base for processing total magnetic field profiles, *Geophysics*, **38**(2), 339–348.
- Gibson, S. A., Thompson, R. N., Leonardos, O. H., Dickin, A. P., & Mitchell, J. G., 1999. The limited extent of plume-lithosphere interactions during continental flood-basalt genesis: geochemical evidence from

- cretaceous magmatism in southern Brazil, *Contributions to Mineralogy and Petrology*, **137**(1), 147–169.
- Golub, G. H. & Loan, C. F. V., 2013. *Matrix Computations (Johns Hopkins Studies in the Mathematical Sciences)*, Johns Hopkins University Press, 4th edn.
- Gomes, C. d. B., Comin-Chiaromonti, P., Azzone, R. G., Ruberti, E., & Rojas, G. E. E., 2018. Cretaceous carbonatites of the southeastern Brazilian Platform: a review, *Brazilian Journal of Geology*, **48**, 317 – 345.
- Hidalgo-Gato, M. C. & Barbosa, V. C. F., 2019. Fast 3d magnetic inversion of a surface relief in the space domain, *Geophysics*, **84**(5), J57–J67.
- Horn, R. A. & Johnson, C. R., 1991. *Topics in Matrix Analysis*, Cambridge University Press, 1st edn.
- Li, W., Lu, W., Qian, J., & Li, Y., 2017. A multiple level-set method for 3d inversion of magnetic data, *Geophysics*, **82**(5), J61–J81.
- Li, Y. & Oldenburg, D. W., 1996. 3-D inversion of magnetic data, *Geophysics*, **61**(2), 394–408.
- Marquardt, D. W., 1963. An algorithm for least-squares estimation of nonlinear parameters, *Journal of the society for Industrial and Applied Mathematics*, **11**(2), 431–441.
- Melcher, G. C. & Coutinho, J. M. V., 1966. Rochas alcalinas e carbonatito de Anitápolis, estado de Santa Catarina, *Boletim da Sociedade Brasileira de Geologia*, **15**(1), 59–93.
- Oliveira Jr., V. C. & Barbosa, V. C. F., 2013. 3-D radial gravity gradient inversion, *Geophysical Journal International*, **195**(2), 883–902.
- Oliveira Jr., V. C., Barbosa, V. C. F., & Silva, J. B. C., 2011. Source geometry estimation using the mass excess criterion to constrain 3-D radial inversion of gravity data, *Geophysical Journal International*, **187**(2), 754–772.
- Pignatelli, A., Nicolosi, I., & Chiappini, M., 2006. An alternative 3d inversion method for magnetic anomalies with depth resolution, *Annals of geophysics = Annali di geofisica*.
- Pilkington, M., 1997. 3-D magnetic imaging using conjugate gradients, *Geophysics*, **62**(4), 1132–1142.
- Pilkington, M., 2009. 3d magnetic data-space inversion with sparseness constraints, *Geophysics*, **74**(1), L7–L15.
- Plouff, D., 1976. Gravity and magnetic fields of polygonal prisms and application to magnetic terrain corrections, *Geophysics*, **41**(4), 727–741.
- Portniaguine, O. & Zhdanov, M. S., 1999. Focusing geophysical inversion images, *Geophysics*, **64**(3), 874–887.
- Portniaguine, O. & Zhdanov, M. S., 2002. 3-D magnetic inversion with data compression and image focusing, *Geophysics*, **67**(5), 1532–1541.
- Reis, A. L. A., Oliveira Jr., V. C., & Barbosa, V. C. F., 2019. *Equivalent layer technique for estimating magnetization direction*, pp. 1769–1773.
- Riccomini, C., Velázquez, V., & Gomes, C., 2005. Tectonic controls of the Mesozoic and Cenozoic alkaline magmatism in the central-southeastern brazilian platform, in *Mesozoic to Cenozoic Alkaline Magmatism in the Brazilian Platform*, chap. 2, pp. 31–55, eds Comin-Chiaromonti, P. & Gomes, C., Edusp/Fapesp, São Paulo.

- Scheibe, L., Furtado, S., Comin-Chiaromonti, P., & Gomes, C., 2005. Cretaceous alkaline magmatism from Santa Catarina state, southern brazil, in *Mesozoic to Cenozoic Alkaline Magmatism in the Brazilian Platform*, chap. 16, pp. 523–571, eds Comin-Chiaromonti, P. & Gomes, C., Edusp/Fapesp, São Paulo.
- Shamsipour, P., Chouteau, M., & Marcotte, D., 2011. 3d stochastic inversion of magnetic data, *Journal of Applied Geophysics*, **73**(4), 336–347.
- Silva, J. B. C. & Hohmann, G. W., 1983. Nonlinear magnetic inversion using a random search method, *Geophysics*, **48**(12), 1645–1658.
- Silva, J. B. C., Medeiros, W. E., & Barbosa, V. C. F., 2001. Potential-field inversion: Choosing the appropriate technique to solve a geologic problem, *GEOPHYSICS*, **66**(2), 511–520.
- Uieda, L., Oliveira Jr., V. C., & Barbosa, V. C. F., 2013. Modeling the earth with fatiando a terra, in *Proceedings of the 12th Python in Science Conference*, pp. 96 – 103.
- Wang, X. & Hansen, R. O., 1990. Inversion for magnetic anomalies of arbitrary three-dimensional bodies, *Geophysics*, **55**(10), 1321–1326.

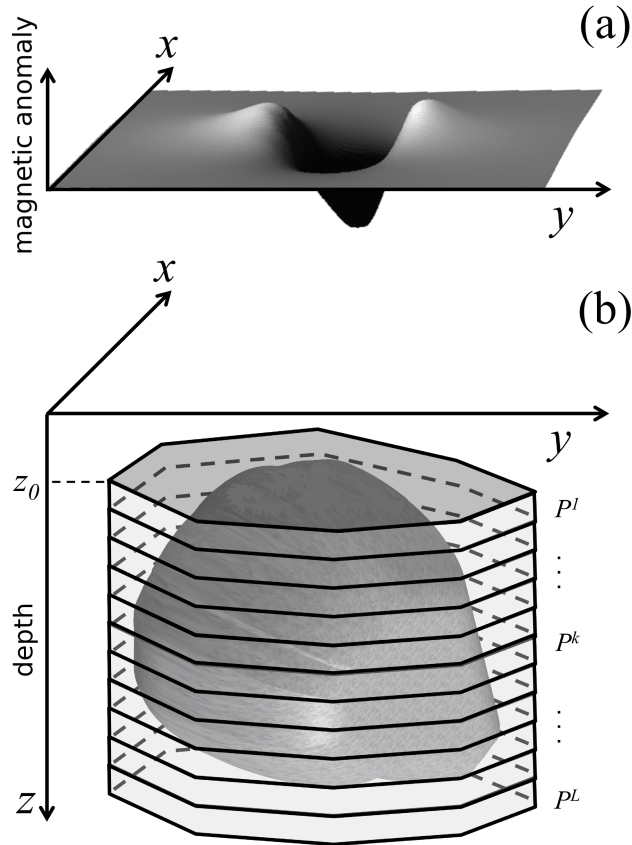


**Figure 1.** Schematic representation the (a) total-field anomaly (gray surface) produced by (b) a 3-D anomalous source (dark gray volume). The interpretation model in (b) consists of a set of  $L$  vertical, juxtaposed prisms (represented in light gray) along the vertical direction.

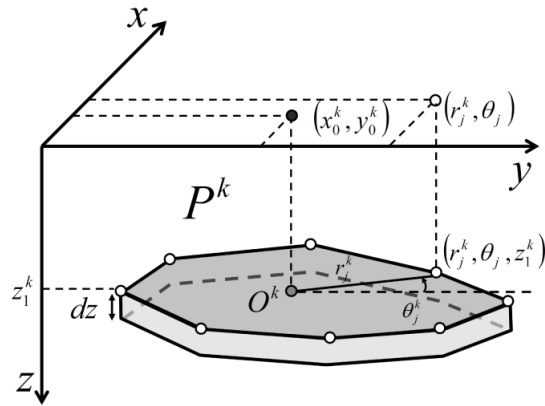


**Figure 2.** Polygonal cross-section of the  $k$ th vertical prism described by  $V$  vertices (white dots) with polar coordinates  $(r_j^k, \theta_j^k)$ ,  $j = 1, \dots, V$ ,  $k = 1, \dots, L$ , referred to an arbitrary origin  $O^k$  (grey dot) with horizontal Cartesian coordinates  $(x_0^k, y_0^k)$ ,  $k = 1, \dots, L$ , (black dot).

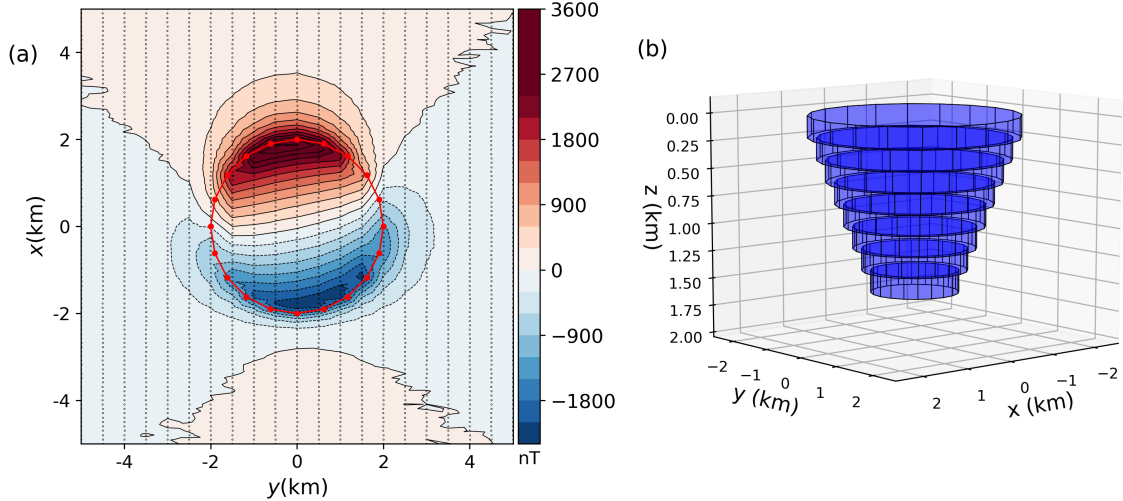


**Figure 3.** Simple model simulation. (a) Noise-corrupted total-field anomaly produced by the lopolithic-like body (blue prisms) shown in the panel (b) with a pseudorandom Gaussian distribution having mean  $\mu_0 = 0$  nT and standard deviation  $\sigma_0 = 5$  nT, the black dots represent the observation points. The connected red dots are the vertices of the initial approximation horizontally projected onto the data map. (b) Perspective view of the simple model (lopolithic intrusion) represented by the blue prisms.

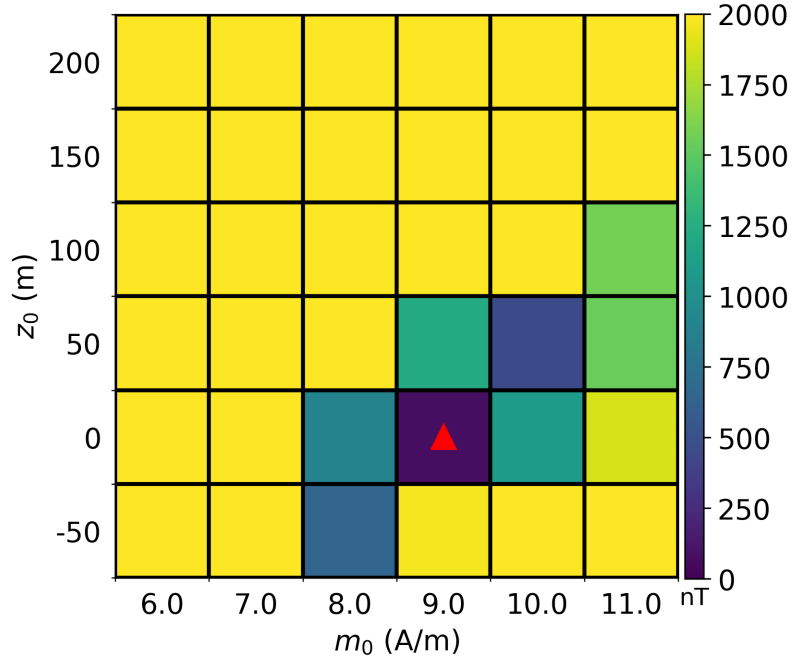


**Figure 4.** Application to the simple model data. Discrete mapping of the goal function  $\Gamma(\hat{\mathbf{p}})$  (eq. 3) on the plane  $m_0 \times z_0$ , produced by estimated models with different depths-to-the-top ( $z_0$ ) and total-magnetization intensities ( $m_0$ ). The red triangle represents the  $m_0$  and  $z_0$  of the true source.

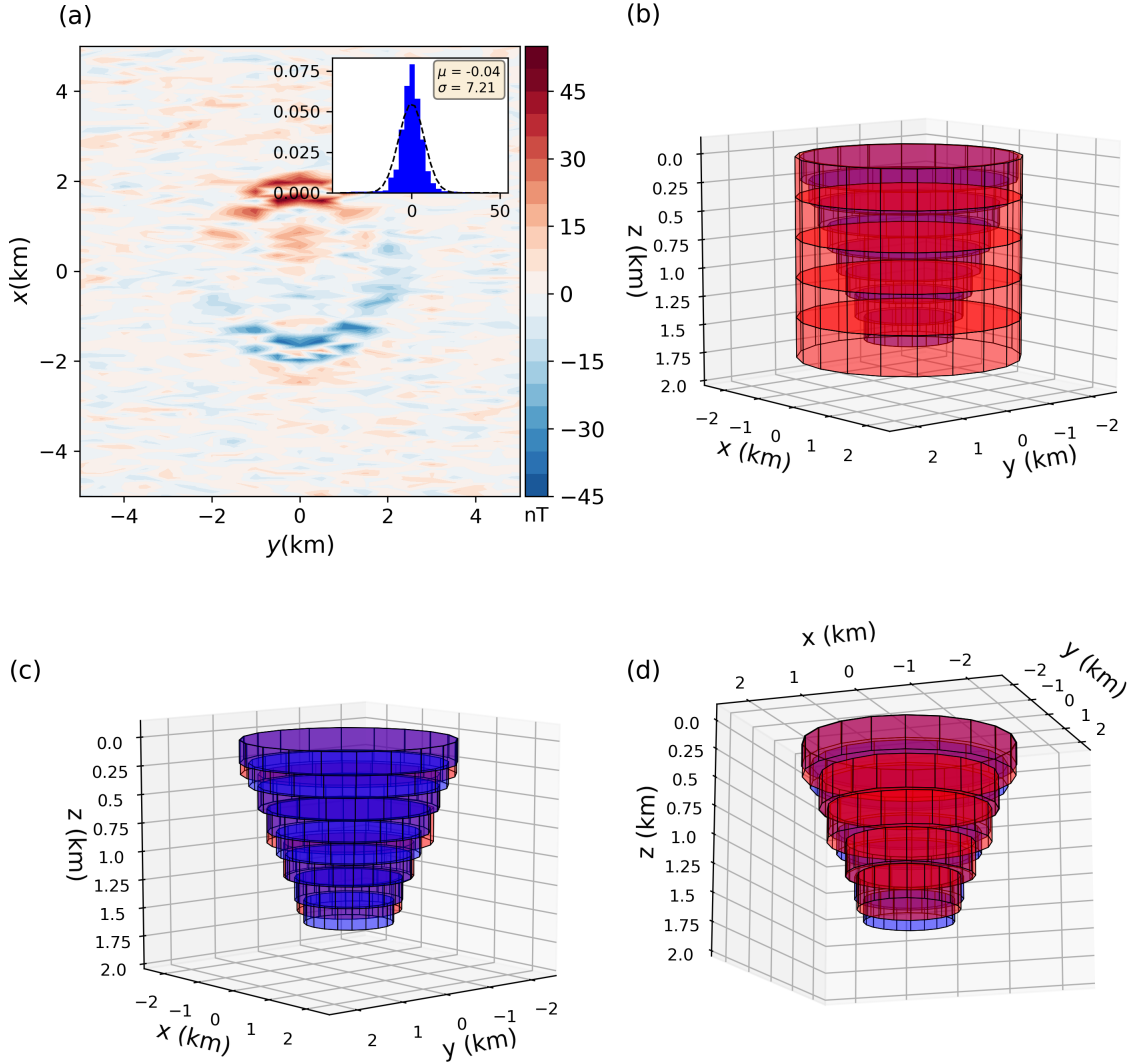


**Figure 5.** Application to the simple model data. (a) Residuals between the noise-corrupted data (Fig. 3a) and the predicted data (not shown) produced by the estimated model (red prisms shown in the panels c and d). The inset in (a) shows the histogram of the residuals and the Gaussian curve (dashed line) whose mean and standard deviation are, respectively,  $\mu = -0.04$  nT and  $\sigma = 7.21$  nT. (b) Perspective view of the initial approximation (red prisms) and the true model (blue prisms). (c) and (d) Comparison between the estimated source (red prisms) and the true model (blue prisms) in perspective views.

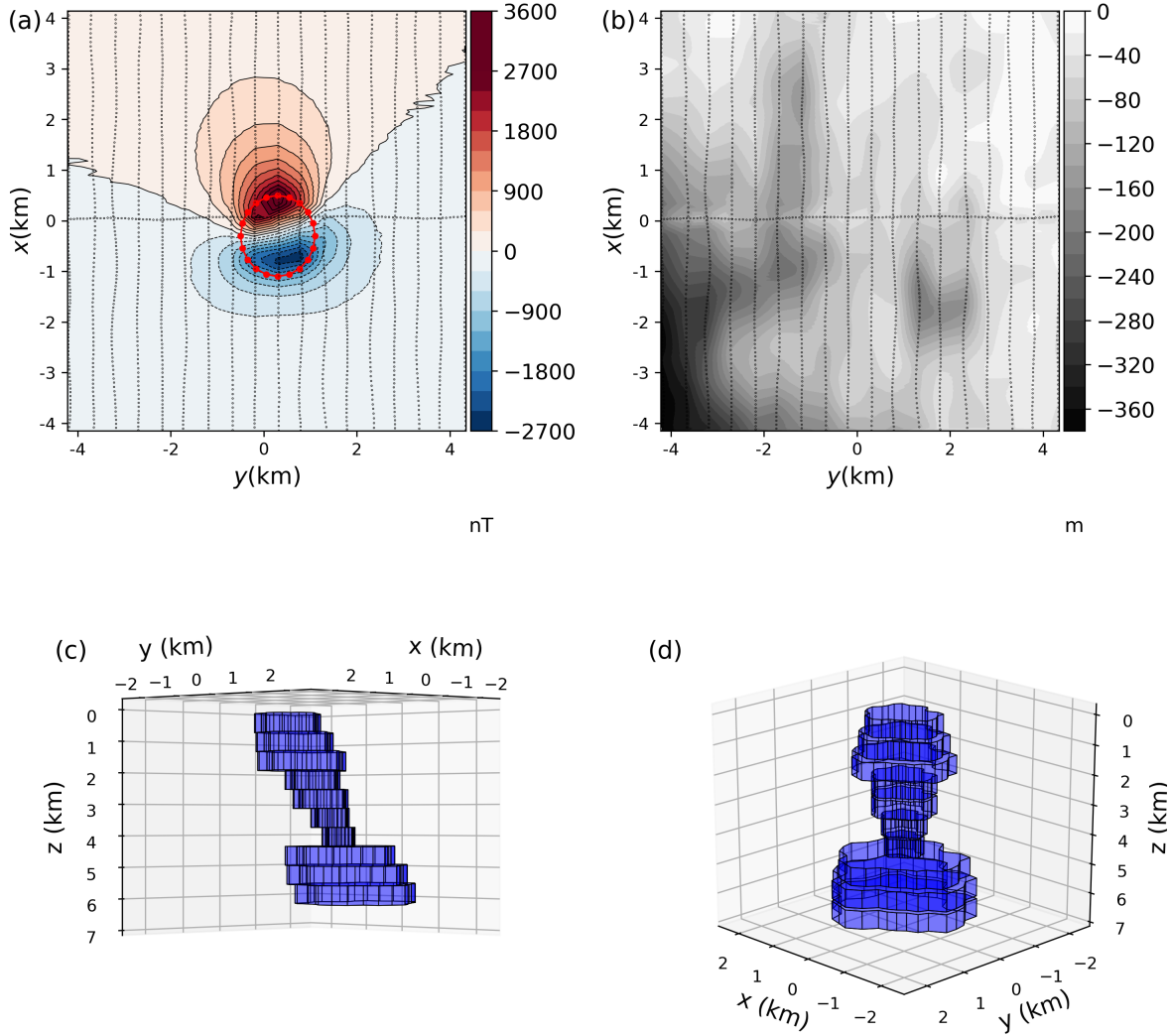


**Figure 6.** Complex model simulation. (a) Noise-corrupted total-field anomaly with a pseudorandom Gaussian distribution having mean  $\mu_0 = 0$  nT and standard deviation  $\sigma_0 = 5$  nT produced by the complex model (blue prisms shown in the panels c and d). The black dots represent the observation points. The connected red dots are the vertices of the initial approximation horizontally projected onto the data map. (b) Vertical coordinates of the observations simulating an airborne survey. (c) and (d) Perspective views of the complex model represented by the blue prisms.

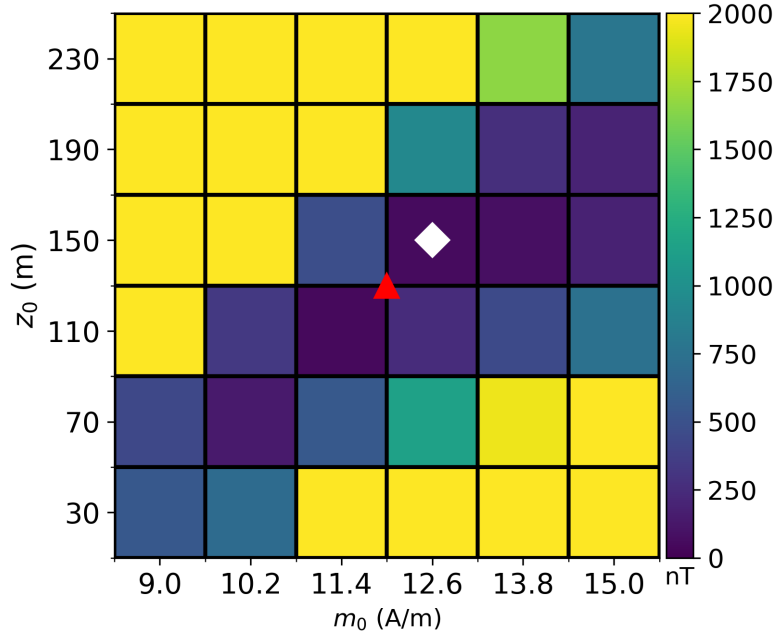


**Figure 7.** Application to the complex model data. Discrete mapping of the goal function  $\Gamma(\mathbf{p})$  (eq. 3) on the plane  $m_0 \times z_0$  produced by estimated models with different depths-to-the-top ( $z_0$ ) and total-magnetization intensities ( $m_0$ ). The red triangle represents the  $m_0$  and  $z_0$  of the true source. The white diamond indicates the estimated pair  $(m_0, z_0)$  that produces the smallest value of  $\Gamma(\mathbf{p})$ .

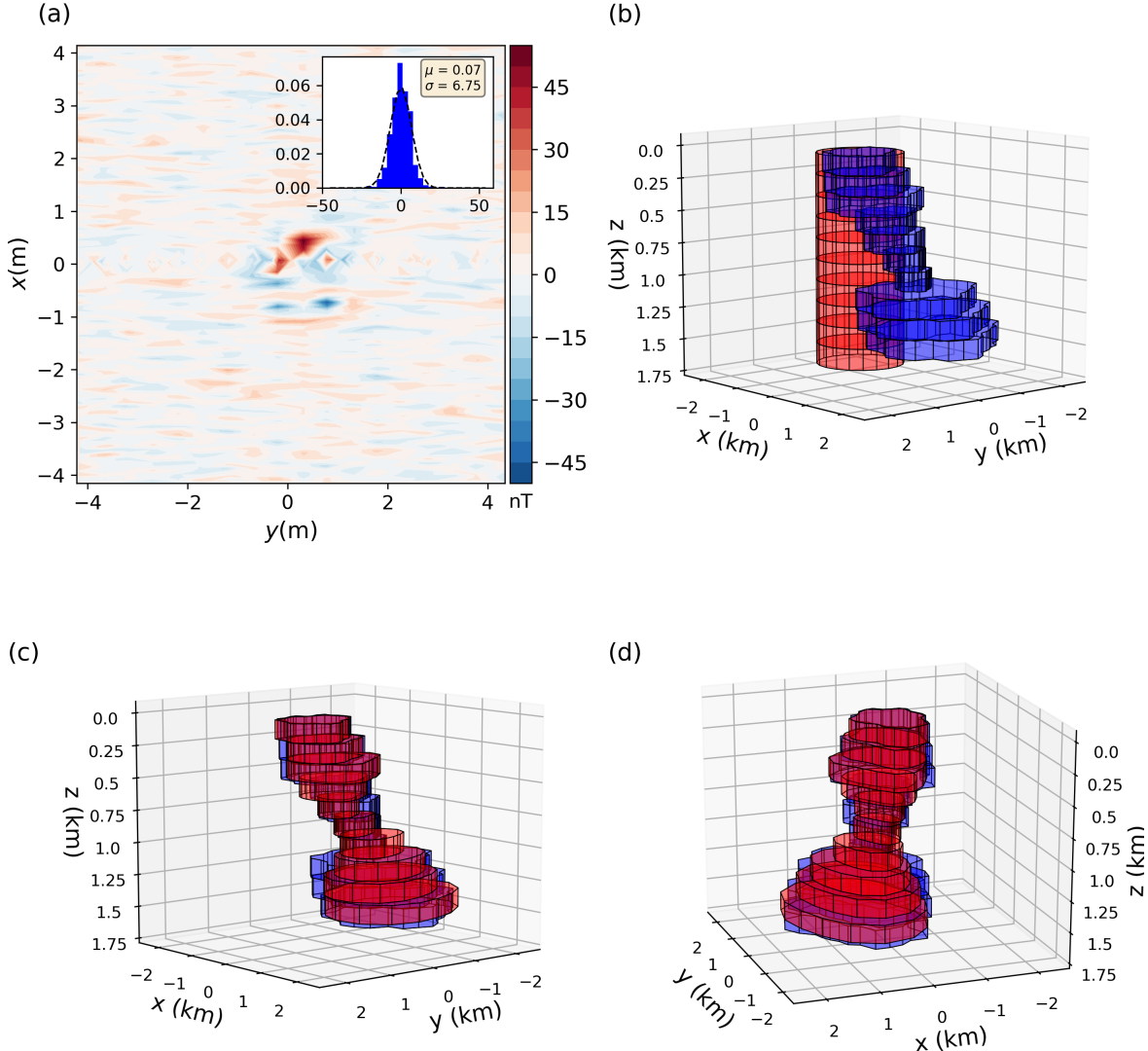


**Figure 8.** Application to complex model data. (a) Residuals between the noise-corrupted data (Fig. 6a) and the predicted data (not shown) produced by the estimated model (red prisms in the c and d panels). The inset in (a) shows the histogram of the residuals and the Gaussian curve (dashed line) whose mean and standard deviation are, respectively,  $\mu = 0.07$  nT and  $\sigma = 6.75$  nT. (b) Perspective view of the initial approximate (red prisms) and the true model (blue prisms). (c) and (d) Comparison between the estimated source (red prisms) and the true model (blue prisms) in perspective views.

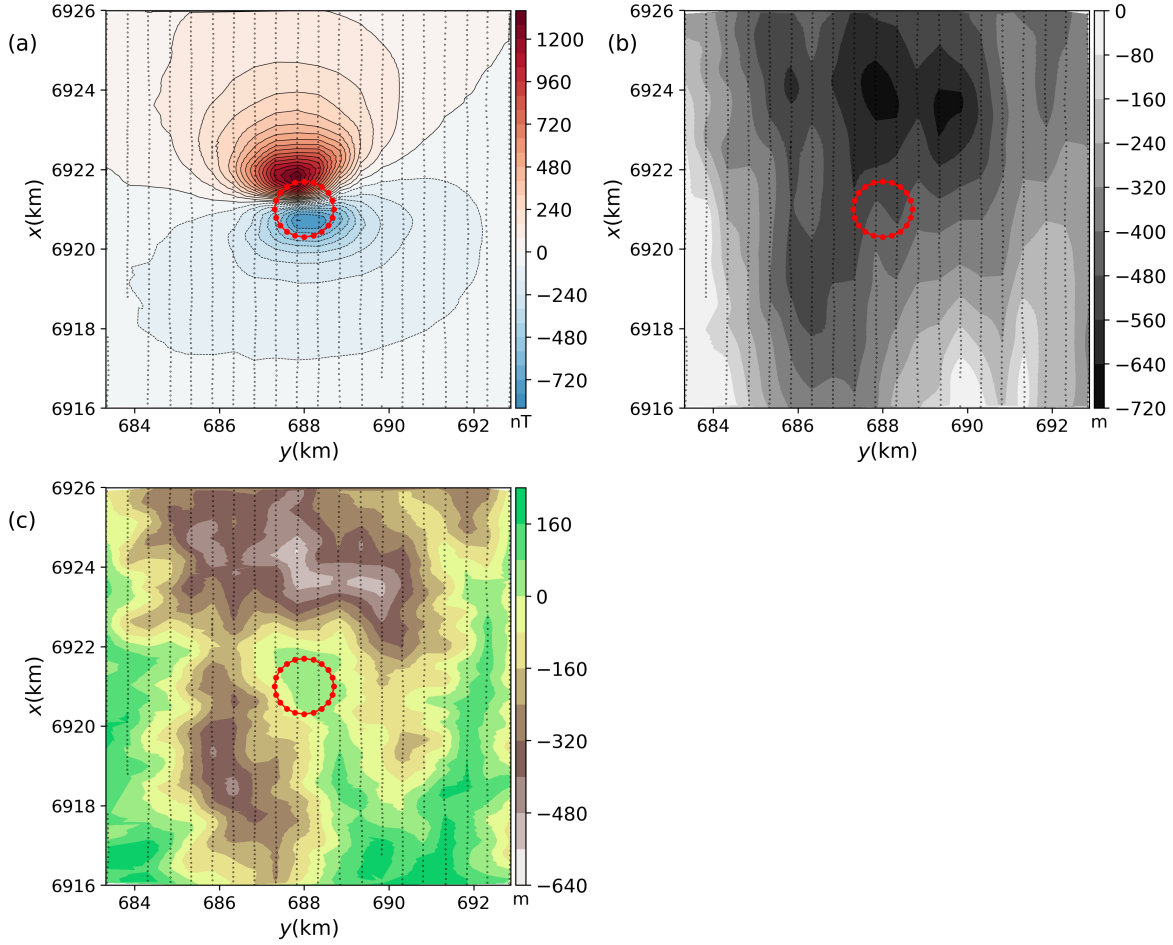


**Figure 9.** (a) Residual total-field anomaly (in nT) over the Anitápolis complex. The horizontal UTM coordinates are referred to the central meridian  $51^{\circ}$  W. (b) and (c) Geometric height of the observation points and the topography, respectively. They are referred to the WGS84 ellipsoid and, for convenience, we have subtracted 800 m from their values. The black dots are the observation points. The connected red dots in both maps are the horizontal projection of the vertices of the initial approximation  $\hat{p}_{(0)}$ .

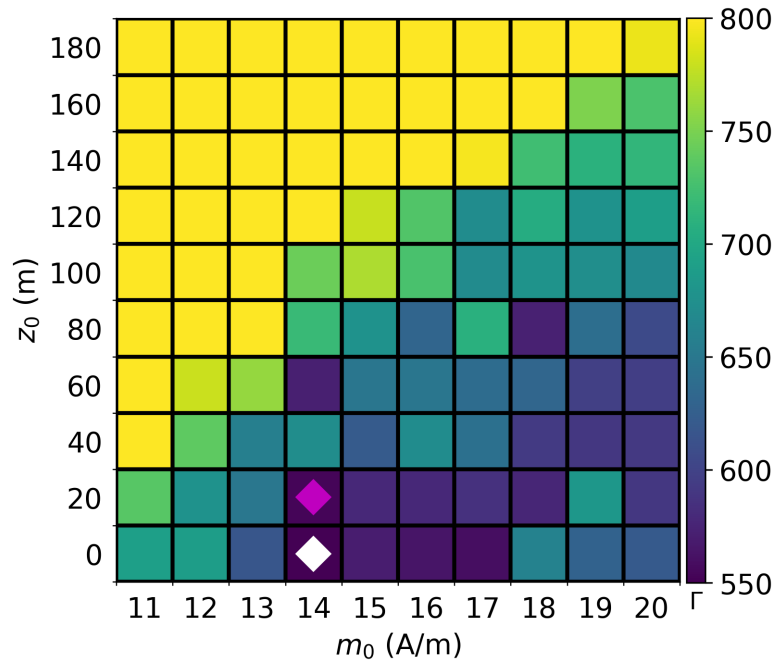


**Figure 10.** Application to the field data over the Anitápolis complex, Brazil. Discrete mapping of the goal function  $\Gamma(\mathbf{p})$  (eq. 3) produced by estimated models with different depths-to-the-top ( $z_0$ ) and total-magnetization intensities ( $m_0$ ). The pink diamond represents the estimated model that produces the smallest value of  $\Gamma(\mathbf{p})$ . The white diamond represents an alternative model whose depth to the top is  $z_0 = 0$  indicating a possible outcropping not corroborated by the literature.

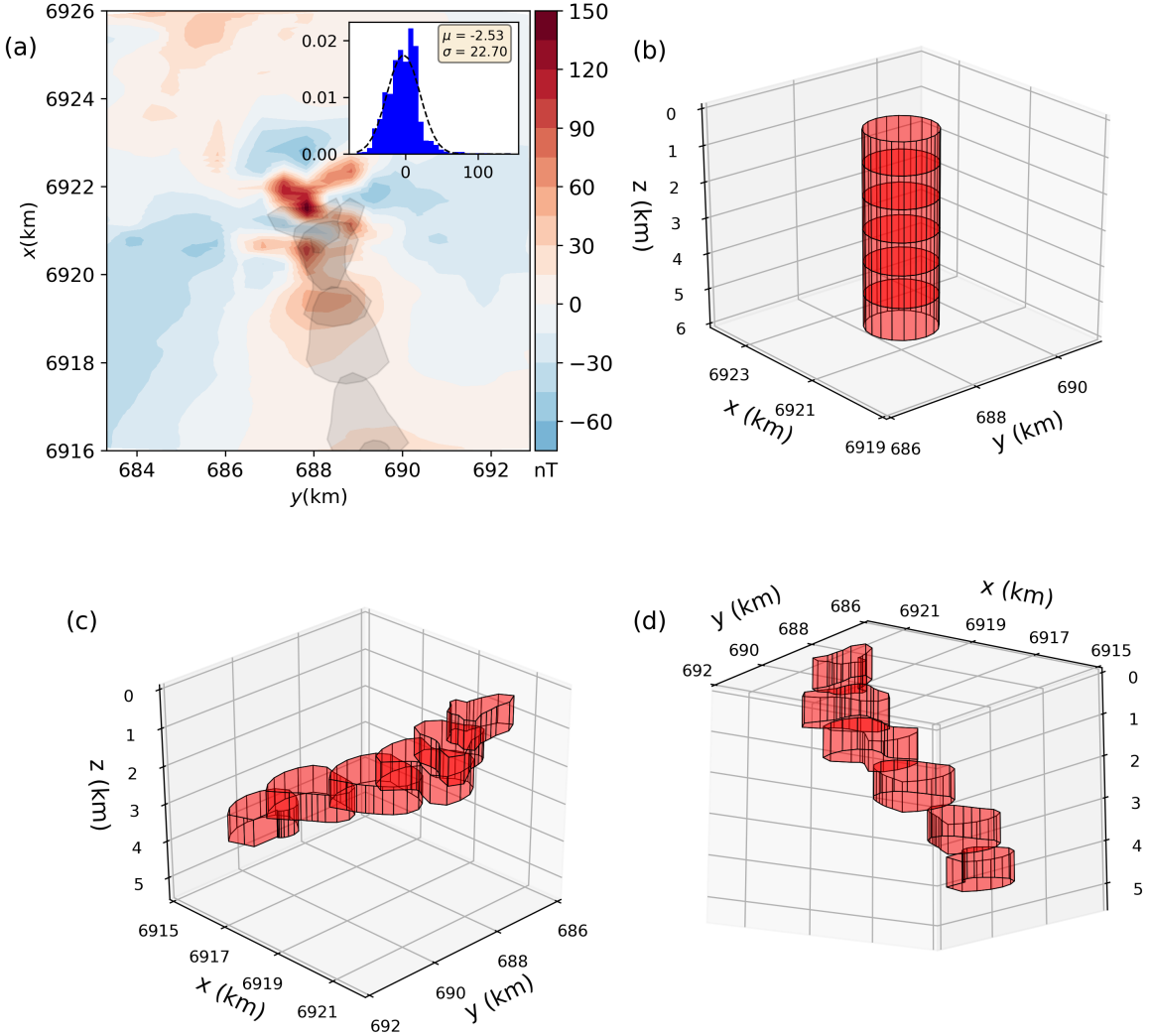


**Figure 11.** Application to the field data over the Anitápolis complex, Brazil. Estimated model producing the smallest goal function value, represented by the pink diamond in Fig. 10. (a) Residuals between the observed data (Fig. 9a) and the predicted data (not shown) produced by the estimated model. The inset shows the histogram of the residuals and a normal Gaussian curve (dashed line) with mean and standard deviation  $\mu = -2.53$  nT and  $\sigma = 22.70$  nT, respectively. The light-gray polygons represent the horizontal projection of the estimated model onto the residual map. (b) Perspective view of the initial approximation (red prisms). (c) and (d) Perspective views of the estimated model (red prisms).

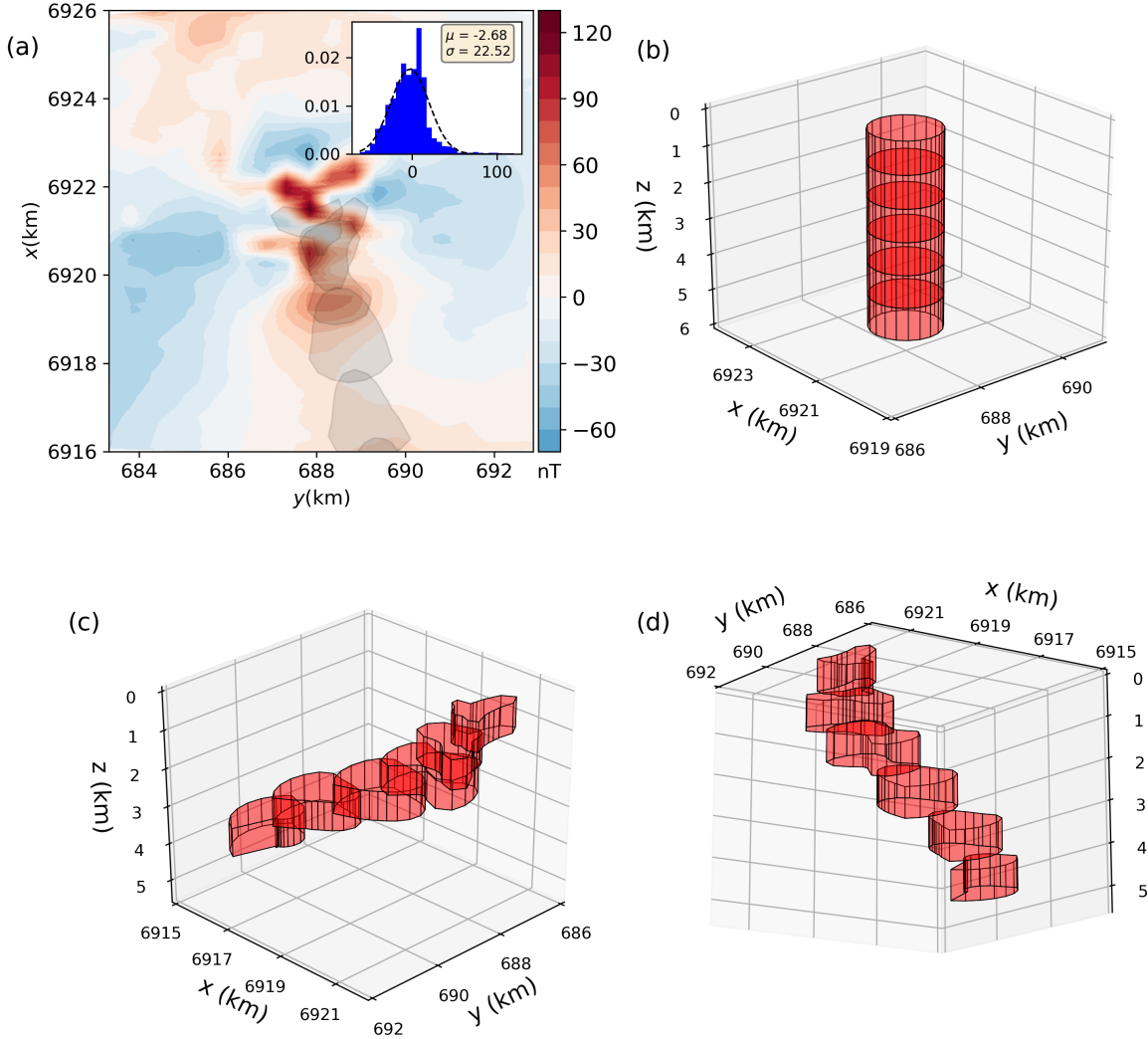


**Figure 12.** Application to the field data over the Anitápolis complex, Brazil. Estimated model with magnetic susceptibility value compatible with a priori information close to the study area, represented by the white diamond in Fig. 10. (a) Residuals between the observed data (Fig. 9a) and the predicted data (not shown) produced by the estimated model. The inset shows the histogram of the residuals and a normal Gaussian curve (dashed line) with mean and standard deviation  $\mu = -2.68$  nT and  $\sigma = 22.52$  nT, respectively. The light-gray polygons represent the horizontal projection of the estimated model onto the residual map. (b) Perspective view of the initial approximate (red prisms). (c) and (d) Perspective views of the estimated model (red prisms).